# Aggregation effects of surface heterogeneity in land surface processes

## Z. Su, H. Pelgrum and M. Menenti

Wageningen UR, ALTERRA Green World Research, P.O.Box 47, 6700 AA Wageningen
e-mail address for corresponding author: su@sc.dlo.nl

## Abstract

In order to investigate the aggregation effects of surface heterogeneity in land surface processes we have adapted a theory of aggregation. Two strategies have been adopted: 1) aggregation of radiative fluxes. The aggregated radiative fluxes are used to derive input parameters that are then used to calculate the aerodynamic fluxes at different aggregation levels. This is equivalent to observing the same area at different resolutions using a certain remote sensor, and then calculating the aerodynamic fluxes correspondingly. 2) Aggregation of aerodynamic fluxes calculated at the original observation scale to different aggregation levels. A case study has been conducted to identify the effects of aggregation on areal estimates of sensible and latent heat fluxes. The length scales of surface variables in heterogeneous landscapes are estimated by means of wavelet analysis.

## Introduction

Land surface processes are heterogeneous at various spatial scales. Since land surface processes are non-linear, and land surface schemes in atmospheric models have a finite (coarse) grid cell size, certain errors will be introduced in attempting to parameterize land-atmosphere interactions. Such errors should ideally be quantified before a model can be used for any predictive purpose, be it for numerical weather prediction (NWPs) or climate research (GCMs). The effects of surface heterogeneity on land-atmosphere interaction can be divided into two categories: aggregation and dynamical effects. Aggregation effects refer to the changes introduced by aggregating different subgrid surface types to the large-scale (grid) average energy and water budgets and land-atmosphere exchanges. Dynamical heterogeneity effects are associated with microscale and meso-scale circulations induced by heterogeneous surfaces, which include both topographic and bio-geophysical heterogeneity. Giorgi and Avissar (1997) have presented a detailed review on both aggregation and dynamical effects. In dealing with subgrid scale heterogeneity, two approaches have been identified, viz the discrete methodology and the probability density function (PDF) methodology. The former treats the model grid as a mosaic of discrete homogeneous subregions so that the calculations are performed separately for each subregion and the aggregation is done as an average over all subregions weighted by their corresponding fractional covers (e.g. Lhomme, 1992; Koster and Suarez, 1992). The latter represents the subgrid scale heterogeneity in variables and parameters via analytical or empirical PDFs and the aggregation is achieved through integrating relevant processes over a phase space defined by the PDFs of the corresponding parameters (e.g. Entekhabi and Eagleson, 1989; Famiglietti and Wood, 1994). Many studies have been conducted in past years, including both empirical and theoretical approaches, employing heuristic models and hypothetical rules (e.g. Mason, 1988; Shuttleworth, 1991, 1998; Lhomme, 1992; Raupach 1992, 1994, 1995; Blyth *et al.*, 1993; Dolman and Blyth, 1997; Shuttleworth *et al.*, 1997). Examinations of the proposed theories or rules have been reported by e.g. Noilhan and Lacarrere (1995), Verhoef *et al.* (1997) and Wang *et al.* (1998). Michaud and Shuttleworth (1997) have presented an executive summary of the Tucson aggregation workshop where various aspects of aggregation have been addressed. Of special relevance to the present work is that by Moran *et al.* (1997) in which the aggregation of temperature and sensible heat flux has been studied for sparse canopies. The same work has also reviewed previous relevant work.

The objective of this study is to deal with the first category of the effects of heterogeneity due to aggregation. Analysis is carried out with remote sensing data collected during the EFEDA field campaign (Bolle *et al.*, 1993).

Specifically, the question to be addressed is: How does the level of aggregation affect surface energy fluxes, as

fluxes are aggregated from the resolution at which they are observed to the coarse grid cell size of the atmospheric model?

# Theory of aggregation

The effects of aggregation will be examined by changes in the pattern of a particular error function defined as the deviation of an aggregated quantity from the original one. Two strategies will be adopted:

(1) Aggregation of radiative fluxes. The aggregated radiative fluxes are used to derive input parameters that are then used to calculate the aerodynamic fluxes at different aggregation levels. This is similar to observing the same area at different resolutions using a specific remote sensor, and then calculating the aerodynamic fluxes correspondingly. This approach is of practical use because of the fixed resolution of remote sensors.

(2) Aggregation of aerodynamic fluxes calculated at the original observation scale to different aggregation levels.

The underlying assumption, common to both strategies, is that the land surface processes are fully characterized at the scale of the original data.

The above problem may be formulated mathematically according to Becker and Li (1995). A surface element (a pixel) observed by a remote sensor is assumed to contain $n$ different homogeneous sub-elements, each sub-element, $i$, being characterized by a surface parameter, $P_i$ (such as temperature, albedo, etc). This parameter is defined from the quantity of interest, $Q_i$, (such as radiance, or a flux), by a model, $M$, which relates $Q_i$ to $P_i$ by the relation

$$P_i = M(Q_i) \qquad (1)$$

For the whole element (pixel) at the observation scale of the remote sensor, the overall quantity $\langle Q \rangle$ (i.e. the measured radiance or a large scale flux) may be described as a function of the $n$ quantities ($i = 1, n$) (i.e. local radiance or local flux) at local scale by

$$\langle Q \rangle = q(Q_1, Q_2, \ldots Q_n), \qquad (2)$$

while the corresponding parameter $\langle P \rangle$ is related to $P_i(i = 1, n)$ by

$$\langle P \rangle = p(P_1, P_2, \ldots, P_n) \qquad (3)$$

At the large scale there exists a model L (which could be inferred from the model M) relating $\langle P \rangle$ to $\langle Q \rangle$ by

$$\langle P \rangle = L(\langle Q \rangle) \qquad (4)$$

Similarly, the terms for aerodynamic fluxes in land-atmosphere interactions (which cannot be observed directly with a remote sensor) can be defined at different scales as

$$\langle F \rangle = f(F_1, F_2, \ldots F_n) \qquad (5)$$
$$F_i = S(P_i) \qquad (6)$$
$$\langle F \rangle = T(\langle P \rangle) \qquad (7)$$

In this investigation, the Surface Energy Balance Algorithm for Land (SEBAL) has been applied (Bastiaanssen, 1995; Menenti and Bastiaanssen, 1997). SEBAL is developed as an algorithm for a pixel-wise calculation of surface heat fluxes from remote sensing data. The algorithm has been improved recently to remedy some theoretical and practical shortcomings (Su et al., 1998). Some details are given in the next section. Consequently, the SEBAL model represents the $S$ function in Eqn. (6).
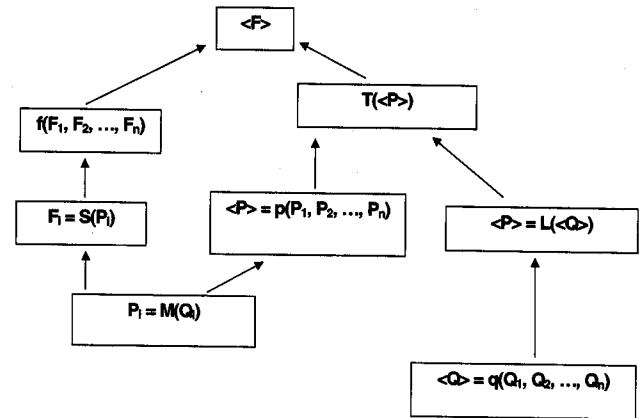


Fig. 1. *The process of aggregation. Left route: aggregation of aerodynamic fluxes. Right route: Aggregation of radiative fluxes. Middle route: aggregation of parameters.*

The whole process of aggregation is shown schematically in Fig. 1. The left route shows the aggregation of aerodynamic fluxes (e.g. sensible and latent heat fluxes) derived from a model ($S$) at local scale, to different resolutions. The aggregation can be done linearly. The right route shows the aggregation of radiative fluxes. The measured radiative fluxes (measured by a remote sensor) are aggregated linearly to different resolutions and the corresponding parameters derived. A model, $T$, is then employed to calculate aerodynamic fluxes at large scale. The aggregation of parameters must be done according to the nature of the parameter concerned and is often non-linear. In this treatment, $S$ and $T$ are identical models (i.e. SEBAL), so that $f$ may be represented by linear averaging. If $q$ and $p$ are average functions and $M$ is a linear function, then $M$ and $L$ become identical. Apparently, by aggregating radiative fluxes and then deriving the corresponding aerodynamic fluxes at different scales, the assumption that $M$ and $L$ are identical is implicit. Where $M$ and $L$ differ, such an aggregation scheme will introduce uncertainties. The middle route is often adopted in practice (e.g. in all current GCMs and large scale SVATs), but is, in most cases, simplified and not accurate due to the non-linearity involved.

In the process of aggregating, only spatially heterogeneous parameters (such as surface albedo, surface temperature, emissivity, vegetation index, incoming global

*Table 1.* Characteristics of the TMS-NS001 data which contain the seven Landsat-TM bands plus a band from 1.13 to 1.35 $\mu$m (band 5). Only the bands corresponding to Landsat-TM bands are used in this study. The TMS-NS001 was on board of NASA's ER2, 29 June 1991, 12.21 GMT, Barrax, Spain, with 18.5m ground resolution ($K(\lambda)$ is the normal incoming spectral solar irradiance and $L_{min}(\lambda)$ and $L_{max}(\lambda)$ are minimum and maximum spectral radiance, respectively).

| Band | Wavelength range $\lambda$ ($\mu$m) | Bandwidth $\Delta\lambda$ ($\mu$m) | $K(\lambda)$ (mw.cm$^{-2}$. $\mu$m$^{-1}$) | $L_{min}(\lambda)$ (mw.cm$^{-2}$.sr$^{-1}$ . $\mu$m$^{-1}$) | $L_{max}(\lambda)$ (mw.cm$^{-2}$.sr$^{-1}$ . $\mu$m$^{-1}$) |
|---|---|---|---|---|---|
| 1 | 0.458–0.519 | 0.07 | 136.93 | −0.15 | 15.21 |
| 2 | 0.529–0.603 | 0.08 | 148.20 | −0.28 | 29.68 |
| 3 | 0.633–0.697 | 0.06 | 92.64 | −0.12 | 20.43 |
| 4 | 0.767–0.910 | 0.14 | 148.64 | −0.15 | 20.62 |
| 6 | 1.57–1.71 | 0.20 | 46.17 | −0.037 | 2.719 |
| 7 | 2.10–2.38 | 0.27 | 14.97 | −0.015 | 1.438 |
| 8 | 10.9–12.3 | 5.50 | 0.0325 | 0.1238 | 1.5600 |

radiation and roughness length) will be considered, while other parameters (such as reference heights etc.) are kept constant. Data obtained with Thematic Mapper Simulator (TMS-NS001) during the EFEDA campaign (Bolle *et al.*, 1993) for the Barrax region in Spain will be used. In addition, radiosonde and surface tower flux, as well as surface radiation measurements are used, where appropriate, to determine regionally constant parameters. These parameters include atmospheric transmissivity, potential air tem-

perature at the blending height and the incoming long wave radiation at the time of the remote sensing data collection. The characteristics of the TMS-NS001 data are given in Table 1. The spatial resolution of the data, 18.5m, is considered sufficiently detailed to characterize the heterogeneity of the surface under study. Figure 2 shows a colour composite of the data. The circular shapes are due to pivot irrigation. Fields and roads can be seen clearly. The two lines running top to bottom in the middle of the image indicate missing data.

## The modified SEBAL

The Surface Energy Balance Algorithm for Land (SEBAL), developed at DLO Winand Staring Centre in the framework of the Mesoscale Climate Hydrology: Earth Observation System (Bastiaanssen, 1995; Menenti and Bastiaanssen, 1997; Roerink and Menenti, 1998; Su and Menenti, 1999) and improved by Su *et al.* (1998) is used in this study. In determining the regional resistance for heat, the potential air temperature at the blending height is derived from either radiosonde data or NWP predictions. The energy balance is described by

$$R_n = G_0 + H + \lambda E \tag{8}$$

where the symbols indicate net radiation, soil heat flux, sensible heat flux and latent flux, respectively.

The net radiation is derived from the radiation balance

$$R_n = K^{\downarrow} - K^{\uparrow} + L^{\downarrow} - L^{\uparrow}$$
$$= (1 - \alpha)K^{\downarrow} + \varepsilon(\varepsilon'\sigma T_a^4 - \sigma T_0^4) \tag{9}$$

where $K^{\downarrow}$, $K^{\uparrow}$, $L^{\downarrow}$, $L^{\uparrow}$, indicate incoming, outgoing short wave and incoming, outgoing long wave radiation respectively, $\alpha$ is the albedo, $\varepsilon'$ and $T_a$ denote apparent air emissivity and temperature, $\varepsilon$ and $T_0$ are surface emissivity and temperature and $\sigma$ is the Stefan-Boltzmann constant.

The sensible heat flux is obtained using a resistance formulation



*Fig. 2. Colour composite of the TMS-NS001 data (band 4,6,3). The TMS-NS001 was on board of NASA's ER2, 29 June 1991, 12.21 GMT, Barrax, Spain, 18.5m ground resolution (862 by 777 pixels or 15.9km by 14.4km, UTM coordinates at upper left corner: easting-568245.18750m, northing-4333005.0m). The circular shapes are due to pivot irrigation.*

$$H = \rho_a C_p \frac{T_0 - T_a}{r_{ah}} \qquad (10)$$

where $\rho_a$ and $C_p$ are the air density and isobaric specific heat, $r_{ah}$ is the resistance for heat transfer between the surface and the reference height at which the air temperature is specified.

The soil heat flux is parameterized by an empirical function

$$G_0 = \frac{R_n \cdot T_0}{\alpha} (0.32\bar{a} + 0.62\bar{a}^2)(1 - 0.98NDVI^4) \cdot 10^{-2} \qquad (11)$$

where $\bar{a}$ is a daily mean albedo value, $NDVI$ is the normalized difference vegetation index (definition given later). Here $T_0$ is expressed in °C.

The latent heat flux is then derived as the residue of the energy balance as

$$\lambda E = R_n - G_0 - H \qquad (12)$$

To determine the sensible heat flux, we need information on both the vertical temperature difference $dT_a = T_0 - T_a$ and the resistance for heat $r_{ah}$, which can be derived by examining the extreme conditions present in the images. Two conditions will be distinguished, namely dry areas and wet areas.

To determine which pixel belongs to a dry area, a linearised theory proposed by Menenti and Bastiaanssen (1989) is used. Surface temperature and the reflectance of non-homogeneous areas are correlated and the relationships can be applied to determine the effective land surface properties (Menenti *et al.*, 1989; Feddes *et al.*, 1989). Using a simple parameterization of the relationship between soil heat flux and net radiation, and by assuming constant net radiation and air temperature, a formal explanation can be given for the observed surface reflectance and temperature. At low reflectance, surface temperature increases with increasing reflectance. In this case, surface temperature may be termed as 'evaporation controlled' because the increase in temperature is a result of the decrease of the evaporation as a consequence of less soil moisture availability. Here, the increase in excess sensible heat flux exceeds the decrease in net radiation due to increase of reflectance. Beyond a certain threshold value of reflectance, surface temperature decreases with increasing reflectance because the soil moisture has decreased to such an extent that no evaporation can take place. Hence, the available energy is used purely to heat up the surface. However, due to the increase of reflectance, the available energy decreases as net radiation decreases (more is reflected away). This process leads to the decrease of temperature with increasing reflectance. Here, the temperature is said to be 'radiation-controlled'. The threshold value can then be used to determine the pixels belonging to dry areas where the reflectance is bigger than the threshold value. A schematic representation is given in Fig. 3.
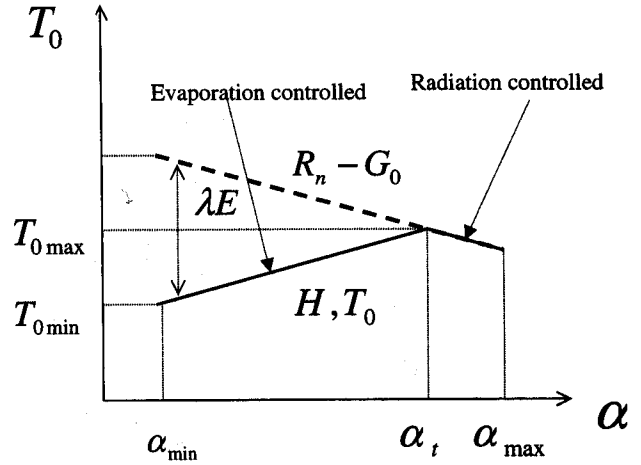
For dry areas, approximately:



Fig. 3. *Schematic representation of the relationship between surface reflectance and temperature: The solid line denotes the relationship between temperature (and also sensible heat) and reflectance, while the dashed line represents the relationship between available energy and reflectance. The difference between the dashed and the solid line gives the latent heat flux according to the energy balance.*

$$\langle \lambda E \rangle \cong 0$$
$$\langle H \rangle \cong \langle R_n - G_0 \rangle$$
$$i.e. \quad \langle R_n - G_0 \rangle = \rho_a C_p \frac{\langle T_0 \rangle - T_a}{\langle r_{ah} \rangle} \qquad (13)$$

For a given regional $T_a$, the area average resistance for heat transfer, $\langle r_{ah} \rangle$, can be derived for the dry areas. Since the above equation has two unknowns, two boundary conditions are required for its solution (one being the dry area assumption, another the given potential regional temperature). This was considered a major theoretical problem in the original formulation of SEBAL in which the role of $T_a$ was ignored and consequently a non-determinant problem was treated as determinant (compare eqn. 7.44, Bastiaanssen, 1995).

Having obtained $\langle r_{ah} \rangle$, the maximum vertical temperature difference, $dT_{a\max}$, is obtained from the equation for sensible heat flux

$$dT_{a\max} = \frac{\langle r_{ah} \rangle}{\rho_a C_p \langle H_{dry} \rangle} \qquad (14)$$

By applying the concept of the blending height (Wieringa, 1986; Mason, 1988), the resistance to heat for each pixel (at a surface reference height) $r_{ah}$ can be obtained. Here the blending height is defined as the height at which the flow is approximately in equilibrium with the local surface and is independent of horizontal position. By aggregating pixel-wise roughness heights, using the heuristic rules of Wood and Mason (1991) and Blyth and Dolman (1995), an effective roughness for dry areas and a regional representative roughness (for the whole area) can be obtained. The former is used to obtain, over dry areas, the effective

friction velocity to derive the wind speed at the blending height. The latter is used, together with the wind speed at the blending height and the local roughness height, to derive the local wind velocity at a near surface reference height (typically 5 metres above the roughness height) for each pixel. With the local wind velocity, the resistance for heat can be derived for each pixel. This latter procedure is a disaggregating process by means of similarity flux profile relationships (Fig. 4) in which the following relationships are utilized (e.g. Brutsaert, 1982)

$$r_{ah} = \frac{1}{ku_*}\left[\ln\left(\frac{z}{z_{0h}}\right) - \Psi_h(z,L) + \Psi_h(z_{0h}, L)\right] \quad (15a)$$

$$u = \frac{u_*}{k}\left[\ln\left(\frac{z}{z_{0m}}\right) - \Psi_m(z,L) + \Psi_m(z_{0m}, L)\right] \quad (15b)$$

$$kB^{-1} = \ln\frac{z_{0m}}{z_{0h}} \quad (15c)$$

$$L = -\frac{\rho_a C_p u_*^3 T_a}{kgH} \quad (15d)$$

where $u$, $u_*$ denote the wind velocity and friction velocity respectively. $\Psi_m(\cdot)$, $\Psi_h(\cdot)$ are the stability corrections for momentum and heat, respectively, and can be described by the Businger-Dyer function for unstable and neutral conditions (Brutsaert, 1982) and the Beljaars-Holtslag expression for stable conditions (Beljaars and Holtslag, 1991a; Van den Hurk and Holtslag, 1995). $L$ is the Obukhov length. $z$, $z_{0m}$, $z_{0h}$ are respectively the reference height, the roughness height for momentum and the roughness height for heat and $k = 0.4$ is the von Kármán constant.

At present, $z_{0m}$ is assigned the value of the roughness value $z_0$ and $z_{0h}$ is derived by assigning the value of 2.3 for

$kB^{-1}$ (Brutseart, 1982). This is clearly an oversimplification of a rather complicated phenomenon that involves different sources for momentum and heat transfers. Quite different ranges of $kB^{-1}$ values have been reported for heterogeneous terrain (Kustas et al., 1989; Beljaars and Holtslag, 1991; Blyth and Dolman, 1995; Wang et al., 1998). Recently the validity of a constant $kB^{-1}$ has again been strongly questioned (Verhoef et al., 1997). Ultimately this value must depend on the flow itself and should be expressed in terms of the roughness Reynolds number (which of course also depends on the flow characteristics). This remains a future research issue.

The wet areas are simply taken as the areas with low reflectance associated with low temperature. For these:

$$\langle \lambda E\rangle \cong \langle R_n - G_0\rangle$$
$$\langle H\rangle \cong 0 \quad (16)$$
$$dTa_{\min} \cong 0$$

On the assumption that the vertical temperature difference is linearly related to the surface temperature, a pixel-wise $dT_a$ can be obtained.

The sensible heat flux is then calculated using $dT_a$ and $r_{ah}$ for each pixel and the latent heat flux results from the residual of the surface energy balance, on the assumption that local advection is non-existent below the surface reference height.

Finally, the evaporative fraction can be obtained as

$$\Lambda = \frac{\lambda E}{H + \lambda E} = \frac{\lambda E}{R_n - G_0} \quad (17)$$

Since $\Lambda$ is a convenient quantity for initialization of soil moisture fields in numerical weather prediction models (Van den Hurk et al., 1997), it is used to evaluate the aggregation effects of surface heterogeneity. To quantify the variability of individual parameters, wavelet analysis will be applied.

## Wavelet analysis for determination of length scales of land surface characteristics

Wavelet analysis is a relatively new tool in geophysics (Kumar and Foufola-Georgiou, 1997). The wavelet transform is closely related to the Fourier transform. Both transforms decompose data into frequencies. The main difference is that the Fourier transform is a global transform, whereas the wavelet transform acts locally. The Fourier transform can tell which frequencies are present in the signal but is unable to distinguish at which location a change in frequency takes place in the data. The wavelet transform uses a local analyzing kernel, and is therefore able to tell at which location a change in frequency takes place. A wavelet $\psi$ is a function which is dilated with a scale parameter, $s$, and translated by $u$, (Mallat, 1998):
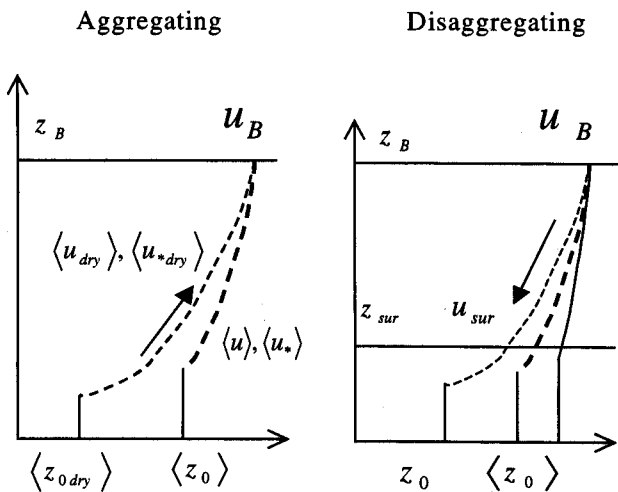


Aggregating        Disaggregating

Fig. 4. *Schematic illustration of the aggregating—disaggregating process—the wind velocity $u_B$ at the blending height $z_B$ is utilized to obtain the wind velocity $u_{sur}$ at the surface reference height $z_{sur}$, which in turn is used to obtain $u_*$, the friction velocity for each pixel (corresponding to the pixel-wise roughness length $z_0$).*

$$\psi_{u,s}(t) = \frac{1}{\sqrt{s}} \psi\left(\frac{t-u}{s}\right) \qquad (18)$$

Note that $t$ can be either spatial or temporal. The wavelet transform of a function $f$, $Wf(u,s)$, at scale $s$ and position $u$ is computed by convolving the wavelet $\psi$ with a function $f$:

$$Wf(u,s) = \int_{-\infty}^{+\infty} f(t) \frac{1}{\sqrt{s}} \psi^*\left(\frac{t-u}{s}\right) dt \qquad (19)$$

The function $f$ can also be replaced by any discrete data set.

In this study, use will be made of the most simple wavelet present, the Haar wavelet:

$$\psi(t) = \begin{cases} 1 & \text{if } 0 \leq t < \frac{1}{2} \\ -1 & \text{if } \frac{1}{2} \leq t < 1 \\ 0 & \text{otherwise} \end{cases} \qquad (20)$$

When $j$ indicates a dyadic scale and $k$ the position in the data set, the Haar wavelet can be defined as follows:

$$\psi_{j,k}(t) = \frac{1}{\sqrt{2^j}} \psi\left(\frac{t - 2^j k}{2^j}\right) \qquad (21)$$

In this study a Discrete Wavelet Transform (DWT) (Lindsay *et al.*, 1996) is used to decompose the data set into an equally large set of wavelet coefficients. Each wavelet coefficient corresponds with a wavelet $\psi$ of scale level $j$ and position $k$. The scaling function $\phi(j,k)$ can be found by inverting every second element of the corresponding wavelet $\psi(j,k)$. As a consequence, the Haar scaling function is 1 for $0 \leq t < 1$ and 0 elsewhere. The coefficient corresponding with the Haar scaling function is, therefore, the mean value for scale $j$ and position $k$. The decomposition of a data set into wavelet and scaling function coefficients is called a multiresolution analysis (Mallat, 1989).

A multiresolution analysis can be used to decompose data into details, smooths and roughs. The details show how much variability is present at each scale level $j$. Details can be found by summation of the products of the wavelet coefficients and wavelets for that particular scale level $j$. The smooths at scale level $j$ can be found by summation of the products of wavelet coefficients and wavelets for all scale levels equal to and larger than scale level $j$. Using Haar wavelets, the smooths correspond with linearly averaged versions of the data set. This feature makes the Haar wavelet a good analysis tool for aggregation studies. Roughs are defined as the difference between the original data set and the smoothed data set.

For the analysis of remote sensing data, the multiresolution should be performed for a 2-D environment. In consequence, the DWT will work in three different directions: vertical, horizontal and diagonal. The wavelet coefficients are a measure of the intensity of the local variations

of the signal, for the scale under consideration. The value of a coefficient will be large when the size of the wavelet is close to the scale of heterogeneity in the signal. The value of a coefficient will be negligible when the local signal is regular for that particular scale (Ranchin and Wald, 1993). The wavelet variance, is thus a natural tool for investigating the spatial scales of variability in remote sensing data (Percival, 1995). The wavelet variance is defined as:

$$\sigma_{y,j}^2 = \frac{n_j}{N}\left(\frac{1}{n_j} \sum_{k=1}^{L} D_{j,k}^2\right) \qquad (22)$$

Where $\sigma_{y,j}^2$ is the sample wavelet variance of data set $y$ at scale $j$, $D_{j,k}$ are the wavelet coefficients at position $k$ and scale $j$ and $N$ is the number of elements in the total data set. The number of data points at scale level $j$ is given by $n_j = N/2^j$. Since wavelet variance divides the total variance present in the landscape scale by scale, the length scales of a given land surface process can be measured by means of wavelet analysis. In this study, the scale level at which the maximum wavelet variance occurs is defined as the length scale of the land surface process under consideration. This information can be used to infer the error in land surface models with a fixed coarse grid cell size. Discrete wavelet transform also indicates the amount of variability present at different scales.

## Results and discussions

### SPATIAL LAND SURFACE PARAMETERS DERIVED FROM AGGREGATION OF RADIATIVE FLUXES

We will now consider the $M$ functions that relate certain remotely observables to the input parameters to SEBAL. Methods for the derivation of these parameters over continental scales have been presented by Su *et al.* (1998).

### SURFACE ALBEDO

Using field measured surface albedo, $\alpha$, Bastiaanssen (1995) found:

$$\alpha = -0.085 + 1.47 r_p \qquad (23)$$

where $r_p$ is the reflectance value at the appropriate height, which, for simplicity, may be called the planetary reflectance. $r_p$ is calculated as follows:

$$r_p(\lambda) = \frac{\pi L(\lambda)}{e_0 K(\lambda) \cos(\theta)} \qquad (24)$$

where $L(\lambda)$ is the measured spectral radiance at wavelength $\lambda$, $e_0$ is the eccentricity factor that takes into account the average and actual earth-sun distances, $K(\lambda)$ is the normal incoming spectral solar irradiance and $\theta$ is the solar zenith angle.

$$L(\lambda) = L_{\min}(\lambda) + (L_{\max}(\lambda) - L_{\min}(\lambda)) \frac{DN(\lambda)}{255} \qquad (25)$$

$L_{\text{mim}}(\lambda)$ and $L_{\text{max}}(\lambda)$ are the minimum and maximum spectral radiance, $DN(\lambda)$ is the recorded digital number. The constants are given in Table 1.

The integrated broad band planetary reflectance is calculated using (Menenti *et al.*, 1989)

$$r_p = \sum w(\lambda) r_p(\lambda) \qquad (26)$$

The weighting factors, $w(\lambda)$, can be calculated using bands 1-4, 6-7 and the information provided in EOSAT Technical Note (1986) and Iqbal (1983).

The aggregated albedo can be obtained by aggregating $L(\lambda)$, thus

$$\langle r_0 \rangle = -0.085 + 1.47 \sum w(\lambda) \frac{\pi \langle L(\lambda) \rangle}{e_0 K(\lambda) \langle \cos(\theta) \rangle} \qquad (27)$$

Figure 5 shows the albedo derived at different aggregation levels by aggregating radiative fluxes. Qualitatively, the circular patterns due to pivot irrigation are discernable till aggregation level at 148 m, above which it becomes increasingly difficult to recognize individual features in the image.

## VEGETATION INDEX

The normalized difference vegetation index (NDVI) is used, which can be calculated as

$$NDVI = \frac{L(\lambda_4) - L(\lambda_3)}{L(\lambda_4) + L(\lambda_3)} \qquad (28)$$

The aggregation of NDVI is given by
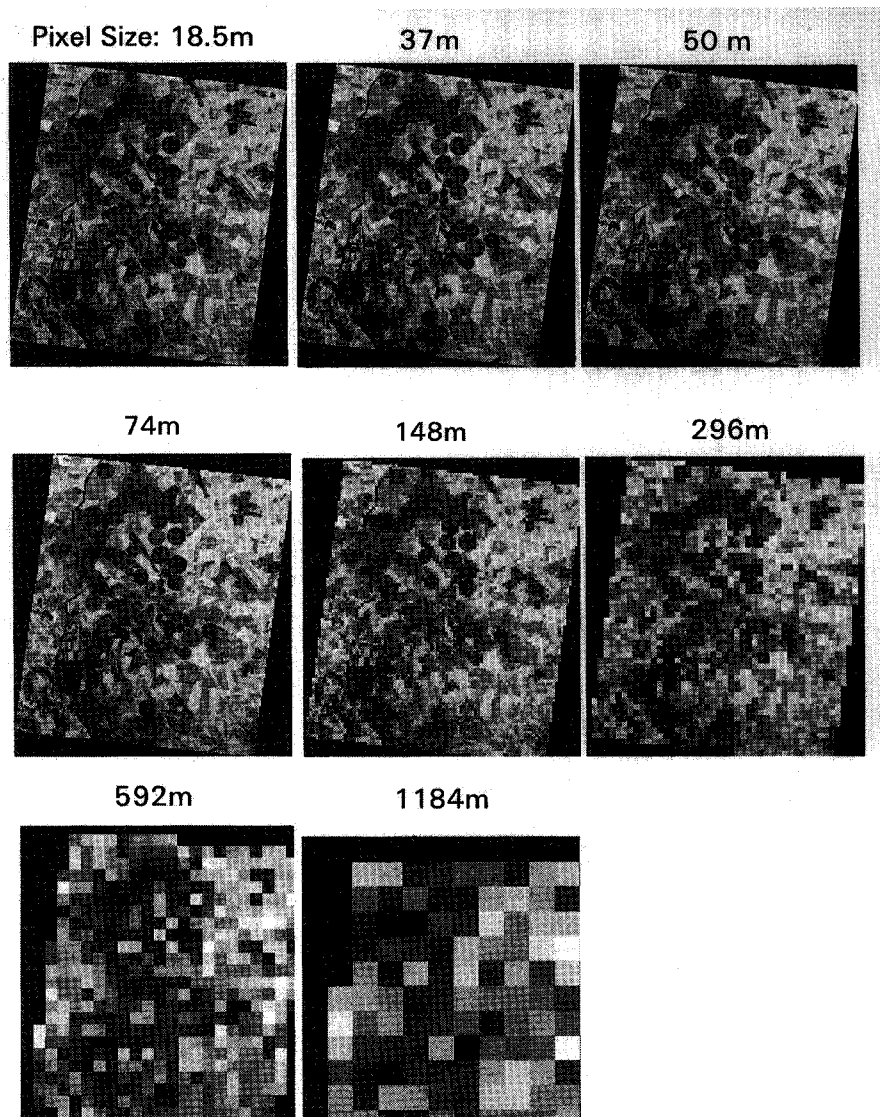


Albedo at different aggregation levels

Fig. 5. *Albedo at different aggregation levels derived by aggregating radiative fluxes (scaled between 0.11 = black and 0.45 = white).*
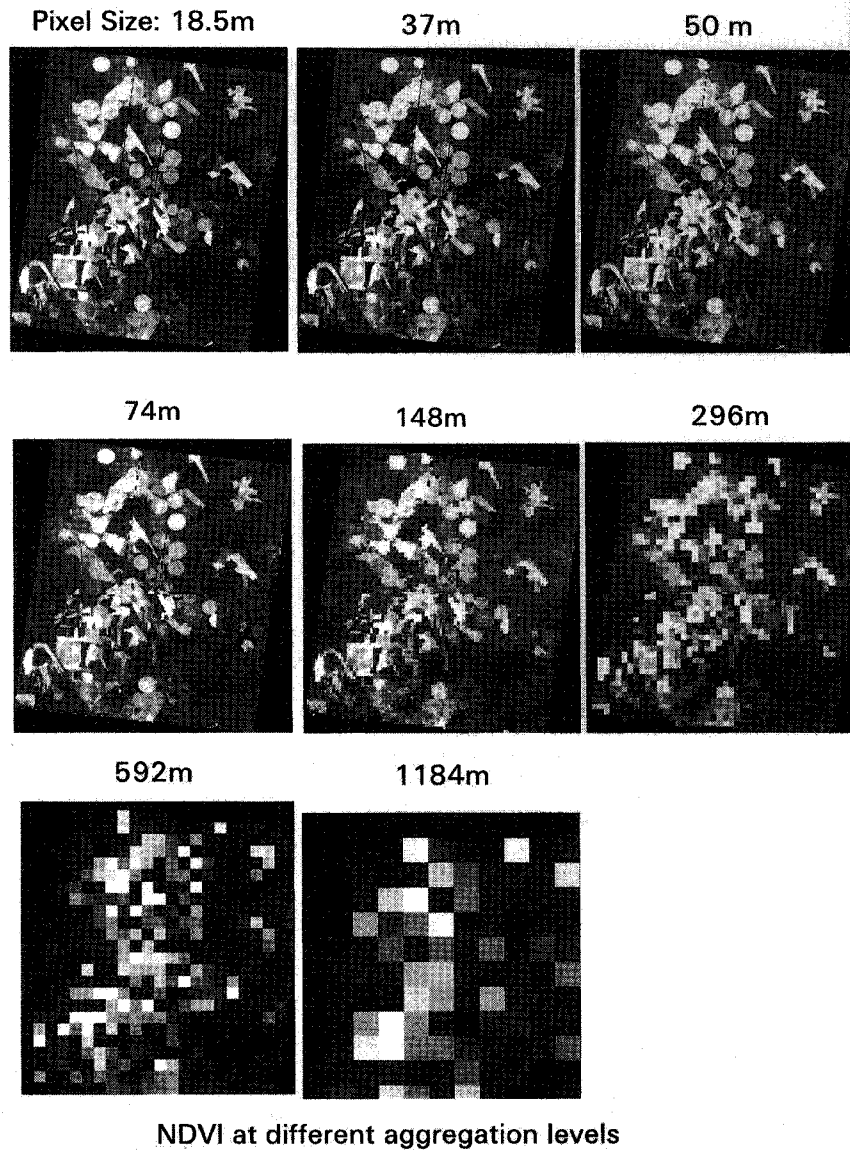
NDVI at different aggregation levels

Fig. 6. *Vegetation index at different aggregation levels derived by aggregating radiative fluxes (scaled between 0.03 = black and 0.99 = white).*

$$\langle NDVI \rangle = \frac{\langle L(\lambda_4) \rangle - \langle L(\lambda_3) \rangle}{\langle L(\lambda_4) \rangle + \langle L(\lambda_3) \rangle} \qquad (29)$$

Figure 6 gives the vegetation index derived at different aggregation levels due to aggregating radiative fluxes. Visually similar conclusions to those for the albedo at different aggregation levels may be drawn for the distribution patterns of different features in the vegetation index images. Quantitative assessment will be given in the discussion following the wavelet analysis.

SURFACE EMISSIVITY

The relationship proposed by Van de Griend and Owe (1993) is used; this reads

$$\varepsilon = 1.009 + 0.047 \ln(NDVI) \qquad (30)$$

which is valid for $NDVI = 0.16 - 0.74$. This equation is empirical and is valid only for the conditions under which the measurements have been made. The conditions in this study are similar to those under which the equation was derived.

Hence

$$\langle \varepsilon \rangle = 1.009 + 0.047 \ln\left( \frac{\langle L(\lambda_4) \rangle - \langle L(\lambda_3) \rangle}{\langle L(\lambda_4) \rangle + \langle L(\lambda_3) \rangle} \right) \qquad (31)$$

The pattern of the surface emissivity derived at different aggregation levels should be similar to that of the vegetation index as given in Fig. 6.

## SURFACE TEMPERATURE

Given the measured thermal infrared radiance, $L_t$, or the converted radiometric temperature, $T_r$, the surface temperature, $T_0$, can be derived from the following equations

$$\varepsilon\sigma T_0^4 = \sigma T_r^4$$
$$\langle \varepsilon\sigma T_0^4 \rangle = \langle \sigma T_r^4 \rangle \qquad (32)$$
$$\langle T_0 \rangle = \left( \frac{\langle T_r^4 \rangle}{\langle \varepsilon \rangle} \right)^{\frac{1}{4}}$$

The radiometric temperature can be derived according to EOSAT Technical Note (1983)

$$T_r = \frac{K_2}{\ln(K_1 / L_t + 1)} \qquad (33)$$

where $K_2 = 1260.56$ mw.cm$^{-2}$.sr$^{-1}$.$\mu$m$^{-1}$ and $K_1 = 60.776$ mw.cm$^{-2}$.sr$^{-1}$.$\mu$m$^{-1}$ are calibration constants.

Figure 7 presents the surface temperature at different aggregation levels due to aggregating radiative fluxes. Similar conclusions may be drawn for albedo and vegetation images at different aggregation levels. However, despite the gross similarities in the distribution of the major patterns in the albedo, vegetation index and temperature images at the different aggregation levels, smaller scale variations may be quite different (e.g. within the pivot irrigation areas). This is because these different parameters represent different aspects of the land surface processes.
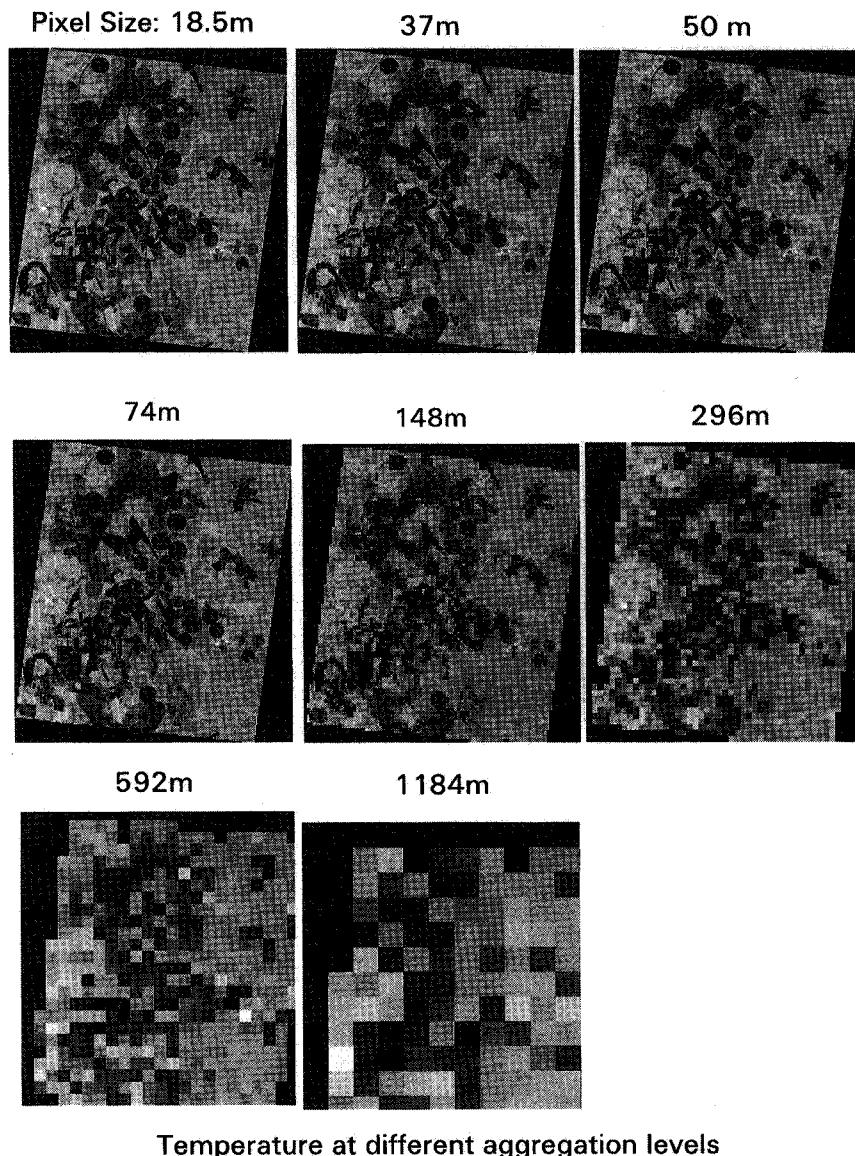
**Pixel Size: 18.5m**      **37m**      **50 m**

**74m**      **148m**      **296m**

**592m**      **1184m**

**Temperature at different aggregation levels**

Fig. 7. *Surface temperature at different aggregation levels derived by aggregating radiative fluxes (scaled between 295 K = black and 319 K = white).*

## INCOMING GLOBAL RADIATION

Incoming global radiation is calculated according to

$$K^{\downarrow} = e_0 I_{sc} \cos(\theta) \cdot \tau_a \qquad (34)$$

where $I_{sc} = 1367$ (w.m$^{-2}$) (Iqbal, 1983) is the solar constant and $\tau_a$ is the total atmospheric transmissivity which can be derived using measured surface incoming global radiation and is assumed spatially constant over the whole region. Hence:

$$\langle K^{\downarrow} \rangle = e_0 I_{sc} \langle \cos(\theta) \rangle \tau_a \qquad (35)$$

Since the study area is small and flat, there will be no big spatial difference in the incoming global radiation field.

## ROUGHNESS LENGTH

Using field measured $z_0$, a relationship was found as (Bastiaanssen, 1995)

$$z_0 = \exp(-5.2 + 5.3 \cdot NDVI) \qquad (36)$$

Since the momentum flux is given by

$$\tau = \rho u_*^2 \qquad (37)$$

where $u_*$ (m.s$^{-1}$) is the friction velocity. Due to the utilization of a blending height in the SEBAL model, $u_*$ becomes spatially constant between a surface reference height (i.e. 5m) and the blending height (i.e. 100m). A parameterization of the aggregated $\tau$ can be expressed as

$$\langle \tau \rangle = \rho \langle u_* \rangle^2 \qquad (38)$$

Under neutral atmospheric conditions, an exact relationship exists between $u_*$ and $z_0$. Such a relationship can guide the aggregation of $z_0$. However, under unstable (which occur most often) and stable conditions, such an analytic expression is impossible to determine due to the stability corrections which are themselves functions of $u_*$. This issue requires further dedicated analysis. Detailed

discussions on the derivation of $z_0$ have been provided by Beljaars and Holtslag (1991b), Wieringa (1993), Menenti and Richie (1994), Mölder (1998), Bosveld et al. (1998) among others.

By assuming that the relationship between $z_0$ and $NDVI$ is valid on all scales (i.e. $M$ and $L$ are identical for $z_0$.):

$$\langle z_0 \rangle = \exp(-5.2 + 5.3 \cdot \langle NDVI \rangle) \qquad (39)$$

The pattern of the roughness length derived at different aggregation levels is similar to the corresponding vegetation index as given in Fig. 6.

## FLUXES AND EVAPORATIVE FRACTIONS OBTAINED BY AGGREGATING RADIATIVE FLUXES

The aggregation was performed up to a pixel size of 1184 m, i.e. scales used in analysis are: 18.5, 37, 50, 74, 148, 296, 592 and 1184 m. Further aggregation appeared impossible since the number of pixels becomes too small to enable statistical estimation of parameters in the SEBAL calculation. The error function to be evaluated is defined as:

$$\Delta = (\langle F \rangle - F) / F \qquad (40)$$

where $\langle F \rangle$ is the aggregated quantity and $F$ is the same quantity at the original scale (18.5 m).

Table 2 shows the statistics of the fluxes calculated at different aggregation levels. Since the evaporative fraction is defined as the ratio of latent heat flux to net radiation minus soil heat flux, taking the ratio may cause the effects due to aggregation to be cancelled out. The statistics of the evaporative fractions are also given in Table 2.

From the table it is immediately obvious that the errors caused by aggregating input parameters are large (between approximately $-10$ to $-30\%$ in $\Lambda$, see Fig. 10). This can certainly be attributed to the non-linearity of the surface processes, but also probably partly to the model formulation.

*Table 2.* Statistics of fluxes and evaporative fraction at different aggregation levels due to aggregating radiative fluxes (m: mean, $\sigma$: standard deviation)

| Scale (m) | Rn (w.m$^{-2}$) | | G0 (w.m$^{-2}$) | | H (w.m$^{-2}$) | | $\lambda E$ (w.m$^{-2}$) | | $\Lambda$ | |
|---|---|---|---|---|---|---|---|---|---|---|
| | m | $\sigma$ | m | $\sigma$ | m | $\sigma$ | m | $\sigma$ | m | $\sigma$ |
| 18.5 | 495.7 | 66.0 | 73.8 | 9.1 | 145.4 | 77.9 | 276.5 | 144.8 | 61.7 | 21.2 |
| 37 | 497.4 | 66.2 | 73.8 | 9.2 | 234.9 | 98.2 | 212.8 | 180.2 | 44.0 | 31.2 |
| 50 | 503.2 | 66.3 | 74.5 | 9.4 | 198.7 | 84.2 | 247.5 | 164.2 | 52.9 | 26.2 |
| 74 | 497.5 | 66.1 | 73.8 | 9.2 | 190.9 | 80.0 | 249.6 | 159.6 | 54.4 | 25.4 |
| 148 | 497.6 | 66.2 | 73.8 | 9.2 | 197.1 | 103.5 | 226.8 | 169.5 | 48.6 | 28.3 |
| 296 | 497.9 | 66.3 | 73.6 | 9.3 | 223.1 | 76.3 | 234.1 | 171.3 | 50.0 | 28.6 |
| 592 | 496.9 | 65.8 | 73.8 | 9.2 | 212.6 | 84.7 | 227.1 | 164.6 | 48.7 | 27.4 |
| 1184 | 500.5 | 67.0 | 73.4 | 9.0 | 185.6 | 73.7 | 247.7 | 148.8 | 53.7 | 23.4 |

Figure 8 shows the evaporative fraction at different aggregation levels. The maps are linearly scaled between 0 = black and 1 = white. The effects of the aggregation can be readily appreciated.

## FLUXES AND EVAPORATIVE FRACTIONS OBTAINED BY AGGREGATING AERODYNAMIC FLUXES

In contrast to the results presented in Table 2, the results in Table 3 show clearly that by aggregating aerodynamic fluxes little error occurred in the final aggregated quantity, whether it is a flux or a ratio (see also Fig. 10). The maps of evaporative fraction are shown in Fig. 9. In terms of the spatial distribution, the patterns at the same aggregation level in Figs. 8 and 9 are similar, but the values differ.

Figure 10 shows the error of evaporative fraction due to different aggregations. The fact that the highest aggregation error occurs in the highest resolution step with the aggregation of the radiative fluxes reveals the complexity of dealing with the aggregation of land surface heat fluxes that are highly non-linear. Specifically, since the way in which the regional resistance is determined using the relationship of surface temperature versus surface reflectance, and due to the non-linear behaviour of this relationship (i.e. with the increase of surface albedo, the surface temperature increases first to a maximum, then decreases as the surface albedo increases further as a consequence of less available net radiation), the outcome of any combination of temperature and albedo at a particular aggregation level is not predictable. Another possible reason could be
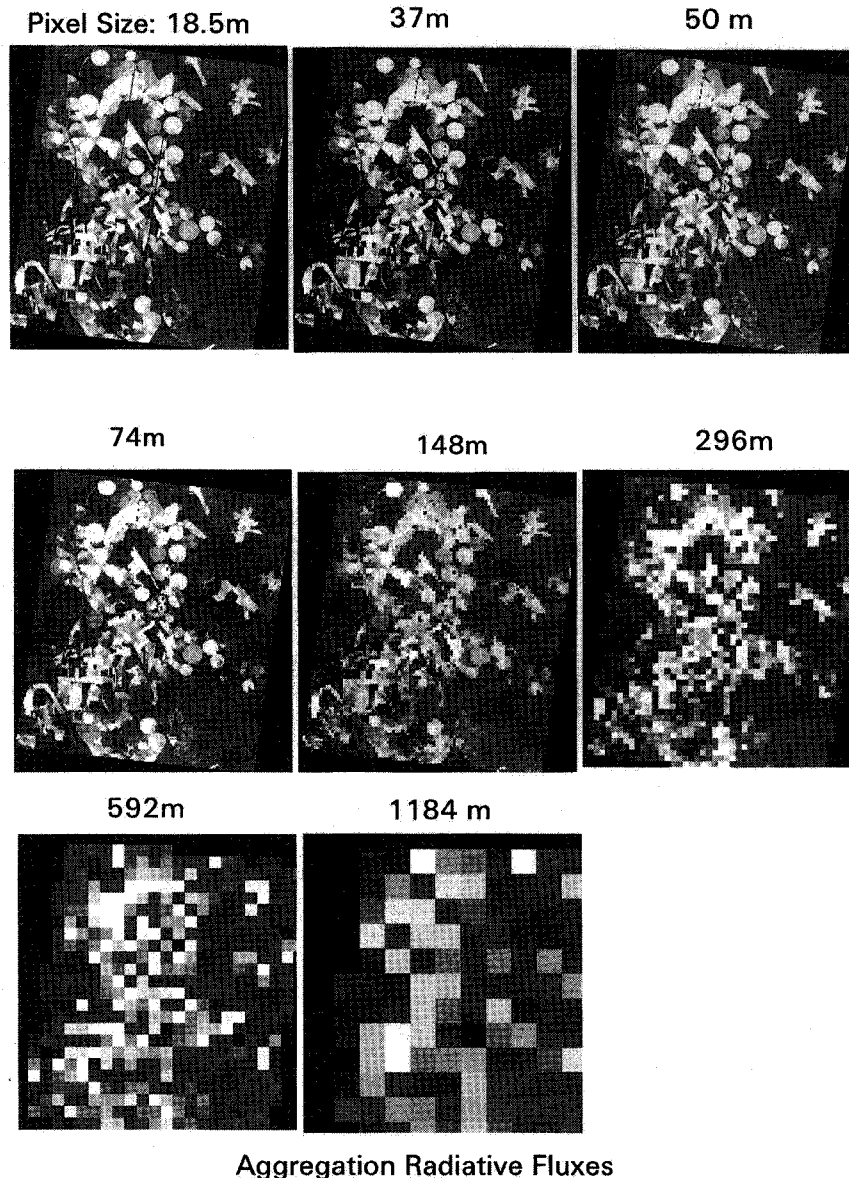


**Aggregation Radiative Fluxes**

Fig. 8. *Evaporative fraction at different aggregation levels due to aggregating radiative fluxes (scaled between 0 = black and 1 = white).*

*Table 3.* Statistics of fluxes and evaporative fraction at different aggregation levels due to aggregating aerodynamic fluxes calculated at the original scale (m: mean, $\sigma$: standard deviation)

| Scale (m) | Rn (w.m$^{-2}$) | | G0 (w.m$^{-2}$) | | H (w.m$^{-2}$) | | $\lambda E$ (w.m$^{-2}$) | | $\Lambda$ | |
|---|---|---|---|---|---|---|---|---|---|---|
| | m | $\sigma$ | m | $\sigma$ | m | $\sigma$ | m | $\sigma$ | m | $\sigma$ |
| 18.5 | 495.7 | 66.0 | 73.8 | 9.1 | 145.4 | 77.9 | 276.5 | 144.8 | 61.7 | 21.2 |
| 37 | 495.8 | 65.3 | 74.0 | 9.0 | 145.6 | 76.5 | 276.5 | 142.9 | 61.8 | 21.0 |
| 50 | 493.7 | 70.4 | 73.5 | 9.8 | 155.1 | 69.1 | 275.4 | 143.9 | 61.6 | 21.0 |
| 74 | 495.7 | 63.9 | 73.9 | 8.8 | 145.5 | 74.3 | 276.5 | 139.5 | 61.9 | 20.4 |
| 148 | 495.8 | 61.2 | 73.8 | 8.4 | 145.4 | 70.4 | 276.6 | 133.3 | 62.2 | 19.6 |
| 296 | 495.8 | 56.7 | 73.8 | 7.6 | 145.2 | 64.0 | 276.8 | 122.5 | 62.6 | 18.2 |
| 592 | 495.6 | 50.1 | 73.8 | 6.5 | 145.6 | 55.3 | 276.2 | 107.2 | 63.0 | 16.2 |
| 1184 | 497.1 | 40.8 | 73.7 | 5.3 | 144.3 | 44.9 | 279.1 | 86.6 | 64.1 | 13.5 |



Aggregation Aerodynamic Fluxes
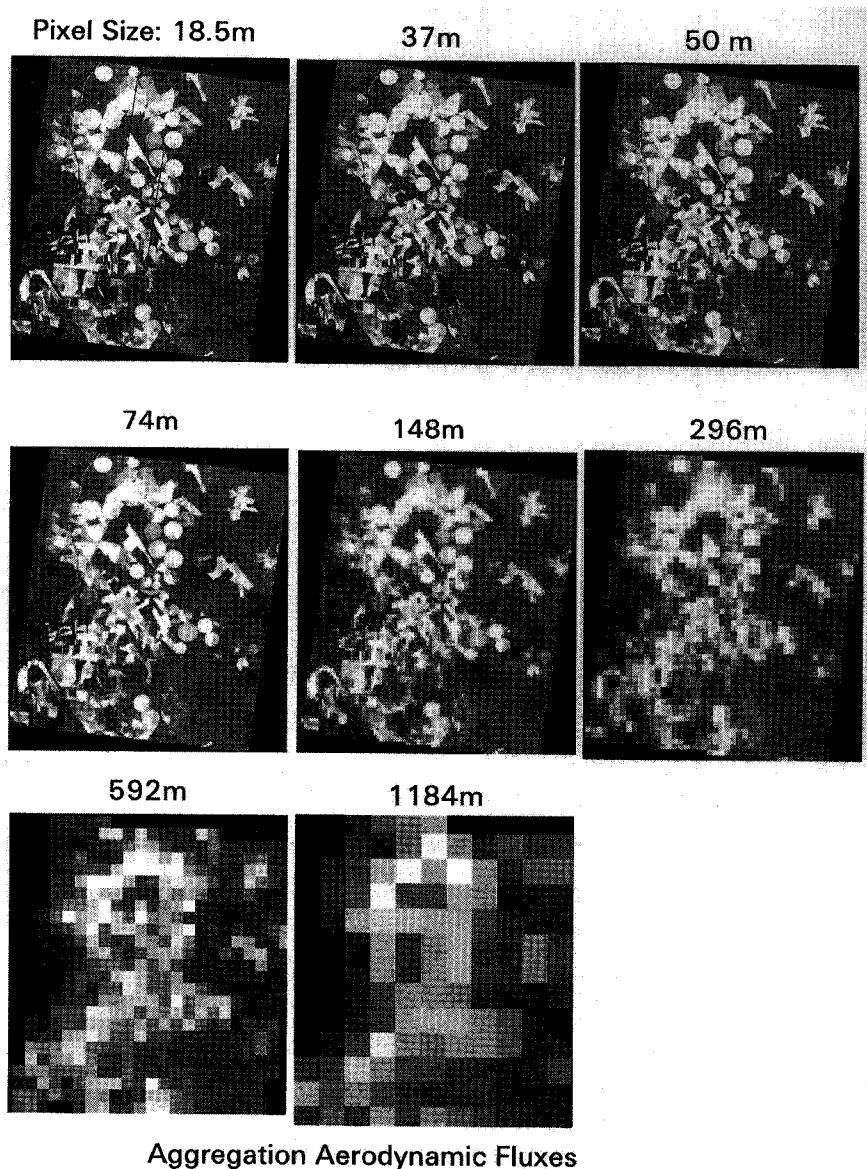
Fig. 9. *Evaporative fraction at different aggregation levels due to aggregating aerodynamic fluxes calculated at the original scale (scaled between 0 = black and 1 = white).*
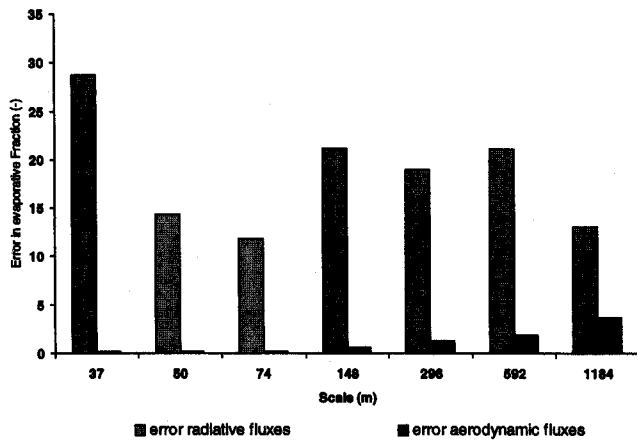
Fig. 10. *Error in estimation of evaporative fraction due to different aggregation methods, calculated from equation (40) with the mean values given in Tables 2 and 3.*

that smaller process scales are not captured by the spatial data presently used. Since the resolution of the original data is 18.5m, processes with scale smaller than about 37m cannot be measured according to sampling theory.

To investigate the further implication of the phenomenon, wavelet analysis has been applied to the surface albedo, temperature, NDVI and evaporative fraction images at the original resolution (18.5m). For the albedo image, the wavelet variance increases gradually with aggregation level to a maximum at 592 m. A similar trend exists for the temperature image, but the highest value is reached at 1184m. The NDVI image has its largest variance also at 1184m (Fig. 11). For the evaporative fraction image, the largest wavelet variance occurs at 592m which, according to the previous definition, is the length scale of the evaporative fraction in this landscape. These characteristics are consistent with the local landscape studied, where the dominant features are the circular pivot irrigation patterns.
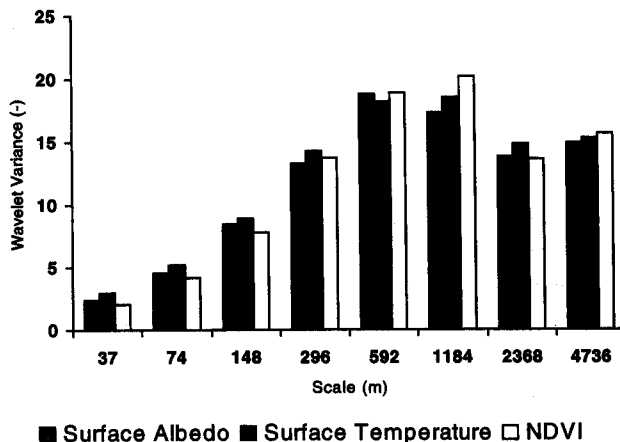


Fig. 11. *Wavelet variance of land surface characteristics.*

## Conclusions

This paper describes a theory for studying the aggregation effects of land surface processes. The modified SEBAL algorithm is employed to convert the input parameters obtained from remotely sensed radiative fluxes to aerodynamic fluxes that cannot be obtained directly from remote observables. For determination of the length scales of the land surface parameters and fluxes, a method based on wavelet analysis is described. With respect to the effects of the level of aggregation on surface energy fluxes, aggregating input parameters by way of aggregating radiative fluxes causes a major uncertainty in calculation of the surface energy balance, while aggregating aerodynamic fluxes obtained at high resolution provides a secure alternative. For this to be correct theoretically, the processes must be captured at a scale smaller than the process scale. Using wavelet analysis, it has been possible to determine the length scale of the land surface studied; this can be explained by the presence of the pivot irrigation patterns in the study area. These conclusions are reached, however, after a study of only one small region and the specific parameterization scheme used to calculate the input parameters and fluxes (i.e. the semi-empirical nature of some of the equations), thus is subject to further verification. To verify the above findings, it is recommended that, during future field campaigns, high resolution images (in the order of 10m) are taken for different landscapes and the procedures developed in this study are applied in the analysis. Also, the images should be large enough that the regional characteristics are represented.

## Acknowledgements

## References

Bastiaanssen, W.G.M., 1995. *Regionalization of surface flux densities and moisture indicators in composite terrain*, Ph.D. Thesis, Agricultural University Wageningen, 273 pp.

Becker, F. and Li, Z.L., 1995. Surface temperature and emissivity at various scales: definition, measurement and related problems, *Rem. Sens. Rev.*, 12, 225–253.

Beljaars, A.C.M. and Holtslag, A.A.M., 1991a. The parameterization of surface fluxes in large scale models under free convection, *Quart. J. Roy. Meterol. Soc.*, 121, 255–270.

Beljaars, A.C.M. and Holtslag, A.A.M., 1991b. Flux parameterization over land surfaces for atmospheric models, *J. Appl. Meteorol.*, 30, 327–341.

Blyth, E.M. and Dolman, A.J., 1995. The roughness length for heat of sparse vegetation, *J. Appl. Meteorol.*, 34, 583–585.

Blyth, E.M., Dolman, A.J. and Wood, N., 1993. Effective resistance to sensible- and latent-heat flux in heterogeneous terrain, *Quart. J. Roy. Meteror. Soc.*, 119, 423–442.

Bolle, H.-J., André, J.C., Arrue, J.L., Barth, H.K., Bessemoulin, P., Brasa, A., de Bruin, H.A.R., Cruces, J., Dugdale, G., Engman, E.T., Evans, D.L., Fantechi, R., Fiedler, F., van de Griend, A., Imeson, A.C., Jochum, A., Kabat, P., Kratzsch, T., Lagouarde, J.-P., Langer, I., Llamas, R., Lopez-Baeza, E., Melia Miralles, J., Muniosguren, L.S., Nerry, F., Noilhan, J., Oliver, H.R., Roth, R., Saatchi, S.S., Sanchez Diaz, J., de Santa Olalla, M., Shuttleworth, W.J., Sogaard, H., Stricker, H., Thornes, J., Vauclin, M., Wickland, D., 1993. EFEDA: European field experiments in a desertification-threatened area, *Ann. Geophys.*, 11, 173–189.

Bosveld, F.C., Holtslag, A.A.M. and van den Hurk, B.J.J.M., 1998. Interpretation of crown radiation temperatures of a dense Douglas-fir forest with similarity theory, *Boundary-Layer Meteorol. (Submitted).* KNMI Preprints 98–14 (Available at: KNMI P.O. Box, 201, NL-3730 AE, De Bilt, NL).

Brutsaert, W., 1982. *Evaporation into the atmosphere,* Reidel, Dordrecht, 299 pp.

Dolman, A.J. and Blyth, E., 1997. Patch scale aggregation of heterogeneous land surface cover for mesoscale meteorological models, *J. Hydrol.*, 190, 252–268.

Entekhabi, D. and Eagleson, P., 1989. Land surface hydrology parameterization for the atmospheric general circulation models including subgrid scale spatial variability, *J. Climate*, 2, 816–831.

EOSAT Tech. Note, 1986. *New look-up tables,* No. 1, 7pp.

Famiglietti, J.S. and Wood, E.F., 1994. Multiscale modeling of spatially variable water and energy balance processes, *Wat. Resour. Res.*, 30, 3061–3078.

Feddes, R.A., Menenti, M. and Kabat, P., 1989. *Modelling the soil water and surface energy balance in relation to climate models,* Proc. European Coord. Meeting in Land Surface processes: Barcelona, 12–15 March, 1989.

Giorgi, F. and Avissar, R., 1997. Representation of heterogeneity effects in Earth system modelling: experience from land surface modeling, *Rev. Geophys.*, 35, 413–438.

Iqbal, M., 1983. *Introduction to solar radiation.* Academic Press, 390 pp.

Koster, R.D. and Suarez, M.J., 1992. A comparative analysis of two land surface heterogeneity representations, *J. Climate*, 5, 1379–1390.

Kumar, P. and Foufola-Georgiou, E., 1997. Wavelet analysis for geophysical applications, *Rev. Geophys.*, 35(4), 385–412.

Kustas, W.P., Choudhury, B.J., Moran, M.S., Reginato, R.J., Jackson, R.D., Gay, L.W. and Weaver, H.L., 1989. Determination of sensible heat flux over sparse canopy using thermal infrared data, *Agric. For. Meteorol.* 44, 197–216.

Lhomme, J.-P., 1992. Energy balance of heterogeneous terrain: Averaging the controlling parameters, *Agric. For. Meteorol.*, 61, 11–21.

Lindsay R.W., Percival, D.B. and Rothrock, D.A., 1996. The discrete wavelet transform and the scale analysis of the surface properties of sea ice, *IEEE Trans. Geosci. Rem. Sens.*, 34, 771–787.

Mallat, S., 1989. A theory for multiresolution signal decomposition: The wavelet representation, *IEEE Trans. Pattern. Anal. Mach. Intel.*, 11, 674–693.

Mallat, S., 1998. *A wavelet tour of signal processing,* Academic Press, 577 pp.

Mason, P.J., 1988. The formation of areally-averaged roughness lengths, *Quart. J. Roy. Meteorol. Soc.*, 114, 399–420.

Menenti, M. and Ritchie, J.C., 1994. Estimation of effective aerodynamic roughness of Walnut Gulch watershed with laser altimeter measurements, *Wat. Resour. Res.*, 30, 1329–1337.

Menenti, M. and Bastiaanssen, W.G.M., 1989. *Estimation of effective properties of non-homogeneous land surfaces with measurements of surface reflectance and temperature.* Proc. 40th Congress, Int. Astronautical Fed. Paris, 7–12 Oct., 1989.

Menenti, M. and Bastiaanssen, W.G.M. (eds.), 1997. *Mesoscale climate hydrology: Earth Observation System-Definition Phase.* Report 106, DLO-Winand Staring Centre, Wageningen, the Netherlands (appeared also as BCRS Report NRSP-2 95–15), 197 pp.

Menenti, M., Bastiaanssen, W.G.M., van Eick, D. and Abd el Karim, M.H., 1989. Linear relationships between surface reflectance and temperature and their application to map actual evaporation of groundwater, *Adv. Space Res.*, 9, 165–176.

Michaud, J.D. and Shuttleworth, W.J., 1997. Executive summary of the Tucson aggregation workshop, *J. Hydrol. (Special Issue)*, 190, 176–181.

Mölder, M., 1998. *Roughness lengths and roughness sublayer corrections in partly forested regions.* Ph.D. dissertation, No. 345, Uppsala University, 45pp.

Moran, M.S., Humes, K.S. and Pinter Jr., P.J., 1997. The scaling characteristics of remotely-sensed variables for sparsely-vegetated heterogeneous landscapes, *J. Hydrol. (Special Issue)*, 190, 337–362.

Noilhan, J. and Lacarrere, P., 1995. GCM grid scale evaporation from mesoscale modelling, *J. Climate*, 8, 206–223.

Percival, D.B., 1995. On estimation of the wavelet variance, *Biometrika*, 82, 619–631.

Ranchin, T. and Wald, L., 1993. The wavelet transform for the analysis of remotely sensed images, *Int. J. Rem. Sens.*, 14, 615–619.

Raupach, M.R., 1992. Drag and drag partition on rough surfaces, *Boundary-Layer Meteorol.*, 60, 375–395.

Raupach, M.R., 1994. Simplified expressions for vegetation roughness length and zero-plane displacement height as functions of canopy height and area index, *Boundary-Layer Meteorol.*, 71, 211–216.

Raupach, M.R., 1995. Corrigenda, *Boundary-Layer Meteorol.*, 76, 303–304.

Roerink, G.J. and Menenti, M. (eds.), 1997. *Climate and hydrology at mesoscale: the contribution of future sensor systems, final report of the bridging phase,* BCRS NUSP 98–01,172pp.

Shuttleworth, W.J., 1991. The Modellion concept, *Rev. Geophys.*, 29, 585–606.

Shuttleworth, W.J., 1998. Combining remotely sensed data using aggregation algorithms, *Hydrol. Earth Sysem Sci.*, 2, 149–158.

Shuttleworth, W.J., Yang, Z.L. and Arain, M.A., 1997. Aggregation rules for surface parameters in global models, *Hydrol. Earth System Sci.*, 1, 217–226.

Su, Z. and Menenti, M. (eds.), 1999. *Mesoscale Climate Hydrology: the contribution of the new observing systems. Pre-Execution Phase, Final Report,* BCRS NUSP-2 99-05, 141pp.

Su, Z., Menenti, M., Pelgrum, H., Van den Hurk, B.J.J.M. and

Bastiaanssen, W.G.M., 1998. Remote sensing of land surface fluxes for updating numerical weather predictions, In Nieuwenhuis, G.J.A., Vaughan, R.A., andMolenaar, M. (eds.), *Operational Remote Sensing for Sustainable Development*, Balkema, 393–402.

Van de Griend, A.A. and Owe, M., 1993. On the relationship between thermal emissivity and the normalized difference vegetation index for natural surfaces. *Int. J. Rem. Sens.* 14, 1119–1131.

Van den Hurk, B.J.J.M., Bastiaanssen, W.G.M., Pelgrum, H. and Van Meijgaard, E., 1997. A new methodology for initialization of soil moisture fields in numerical weather prediction models using METEOSAT and NOAA data, *J. Appl. Meteorol.*, 36, 1271–1283.

Van den Hurk, B.J.J.M and Holtslag, A.A.M., 1995. On the bulk parameterization of surface fluxes for various conditions and parameter ranges, *Boundary-Layer Meteorol.*, 82, 199–134.

Verhoef, A., McNaughton, K.G. and Jacobs, A.F.G., 1997. A parameterization of momentum roughness length and displacement height for a wide range of canopy densities, *Hydrol. Earth System Sci.*, 1, 81–91.

Wang, J.M., Bastiaanssen, W.G.M., Ma, Y.M. and Pelgrum, H., 1998. Aggregation of land surface parameters in the oasis-desert systems of north-west China, *Hydrol. Process.*, 12, 2133–2147.

Wieringa, J., 1986. Roughness-dependent geographical interpolation of surface wind speed averages, *Quart. J. Roy. Meteorol. Soc.*, 112, 867–889.

Wieringa, J., 1993. Representative roughness parameters for homogeneous terrain, *Boundary-Layer Meteorol.*, 63, 323–363.

Wood, N. and Mason, P.J., 1991. The influence of static stability on the effective roughness lengths for momentum and heat transfer, *Quart. J. Roy. Meteorol. Soc.*, 117, 1025–1056.